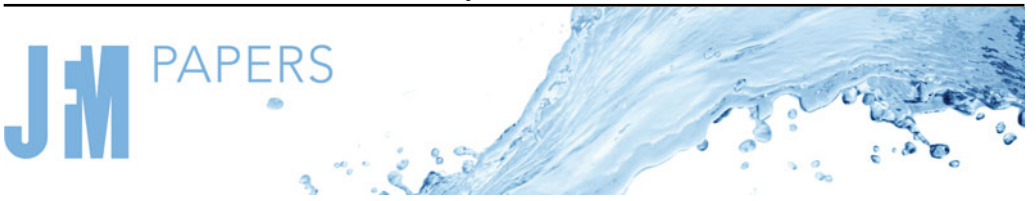
J. Fluid Mech. (2026), *vol.* 1035, A16, doi:10.1017/jfm.2026.11571



On-demand nuclei seeding in Venturi flows – why hydrodynamic cavitation favours attached cavities

Zehao Li[1], **Patricia Pfeiffer**[1] **and Claus-Dieter Ohl**[1]

[1]Department Soft Matter, Institute for Physics, Otto-von-Guericke-University Magdeburg, Magdeburg 39106, Germany

Corresponding author: Zehao Li, zehao.li@ovgu.de

(Received 3 November 2025; revised 31 March 2026; accepted 18 April 2026)

Attached cavitation is likely the most common form of developed hydrodynamic cavitation, yet the reason for its dominance remains unclear. From the experimental side, a natural approach is to seed controllable nuclei and observe their evolution. We propose a laser-based on-demand nucleation method that generates micro- and nanobubbles as nuclei in Venturi flows, enabling unprecedented spatio-temporal control of hydrodynamic cavitation inception. For single-bubble cases, we find that attached cavitation occurs when the bubble surface enters the boundary layer of the channel where the pressure is below the vapour pressure. Based on it, we construct a phase diagram of cavitation regimes as a function of cavitation number and non-dimensional wall distance. Extending to multiple bubbles, assuming a random spatial distribution of nuclei within the laser-illuminated region, we develop a simple model to estimate the probability of attached cavitation. Results show that, at typical cavitation numbers, only a few bubbles suffice for attached cavitation to occur with nearly 100 % probability. Our finding provides new insights into why nuclei in hydrodynamic processes tend to develop into attached cavitation.

Key words: cavitation, multiphase flow

1. Introduction

Cavitation refers to the phase change from liquid to vapour caused by a drop in pressure. Hydrodynamic cavitation denotes cavitation induced by liquid flows. Among various types of hydrodynamic cavitation, attached cavitation is one of the most common forms.

© The Author(s), 2026. Published by Cambridge University Press. This is an Open Access article, distributed under the terms of the Creative Commons Attribution licence (https://creativecommons.org/licenses/by/4.0/), which permits unrestricted re-use, distribution and reproduction, provided the original article is properly cited.

https://doi.org/10.1017/jfm.2026.11571 Published online by Cambridge University Press

It typically appears as a vapour cavity that remains attached to the wall with an unstable tail, leading to periodic shedding and collapse of bubble clouds (Franc & Michel 1985). The cyclic growth and collapse of the attached cavity result in a range of rich phenomena, such as strong pressure waves and micro-jets (Dular & Petkovšek 2015), luminescence (Leighton *et al.* 2003) and the formation of reactive radicals (Nöpel & Ayela 2023). Because of these effects, attached cavitation plays crucial roles in many industrial processes, including fluid machinery erosion (Arndt 1981), mineral flotation (Li *et al.* 2022) and water treatment (Šarc *et al.* 2017).

Despite its common occurrence and significance, the reason why hydrodynamic cavitation tends to appear in the form of attached cavitation is still not fully understood. Previous studies have highlighted its strong connection with the flow boundary layer, where the cavity can remain attached within the low-momentum region with laminar separation or large adverse pressure gradients (Franc & Michel 1985; Ram, Agarwal & Katz 2020). Outside the boundary layer, nuclei experience a more direct evolution process: they expand into isolated vapour bubbles that travel downstream with the main flow – commonly referred to as travelling cavitation bubbles (Chatterjee & Arakeri 2004). Nevertheless, usually, the final cavitation pattern is dominated by attached cavitation, except in certain special flow conditions, such as flows with strong vortices (Pennings *et al.* 2015) or very small adverse pressure gradients (Li, Zuo & Qian 2023), where other patterns prevail. This raises a question: What happens from nucleation to developed cavitation that results in the dominance of attached cavitation? From the experimental side, a straightforward approach to addressing this question is to introduce controllable nuclei into the flow and track their evolution, thereby allowing direct and systematic observation of how hydrodynamic cavitation develops from its very inception.

To date, methods for controllable nucleation in hydrodynamic cavitation experiments remain relatively limited. The most commonly used approach involves introducing microbubbles with partially controlled size and concentration upstream of the low-pressure region, allowing them to be convected into the region of interest. Such microbubbles are typically generated through capillary injection (Agarwal *et al.* 2023), ultrasound excitation (Chatterjee & Arakeri 2004) or the collapse of focused laser-induced cavitation bubbles (Li & Ceccio 1996). These methods have enabled relatively direct observations of nucleation in specific flow patterns (Allan *et al.* 2025) and how nuclei influence the developed cavitation (Venning, Pearce & Brandner 2022). However, since the aforementioned nucleation methods do not generate nuclei *in situ* at the cavitation inception site, further improvement in spatio-temporal resolution – particularly temporal precision – is hindered, which limits the ability to perform rapid and detailed observations of cavitation nucleation.

In this study, we develop a laser-based on-demand nucleation technique within a Venturi flow. A pulsed laser sheet is used to illuminate the region of interest. The inevitably present tiny contaminants in the water are rapidly heated upon absorbing the laser energy, leading to the formation of micro- and nanobubbles (Rosselló & Ohl 2023) that serve as nuclei for hydrodynamic cavitation. Owing to the extremely high spatio-temporal controllability of the laser, both the location and timing of nucleation in hydrodynamic cavitation can be precisely controlled in an unprecedented manner. Based on this technique, we first examine single-bubble cases and obtain a phase diagram of cavitation regimes. Extending to multiple-bubble cases, we developed a simple theoretical model to estimate the probability of attached cavitation. We found that, at typical cavitation numbers, only a few bubbles are sufficient for the probability of attached cavitation to approach nearly 100 %.

https://doi.org/10.1017/jfm.2026.11571 Published online by Cambridge University Press

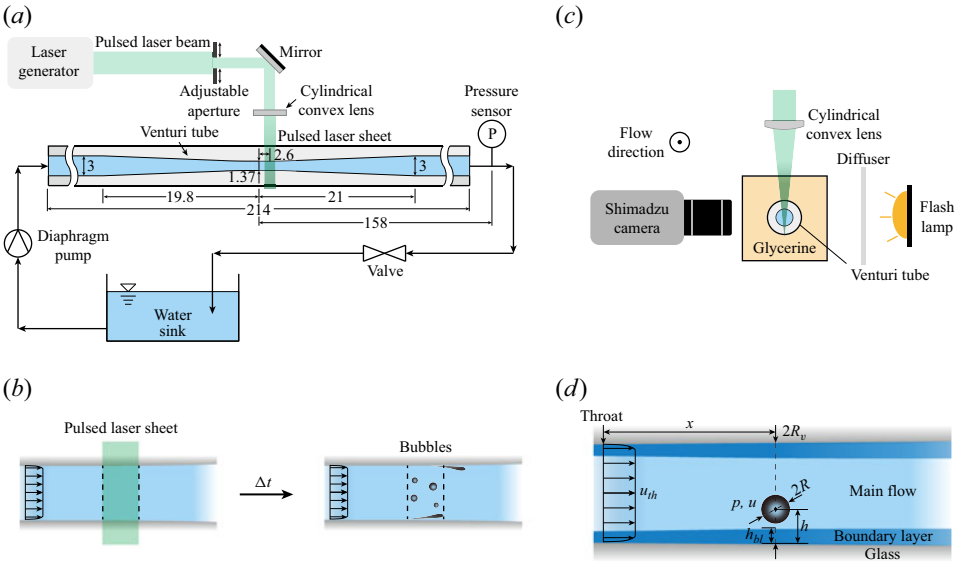


Figure 1. Description of the experimental set-up (not to scale, the unit of all length labels in mm). (*a*) Hydraulic system and laser set-up from the front view. (*b*) Schematic of the nuclei seeding by a pulsed laser sheet in the Venturi flow. (*c*) Laser and high-speed photography set-up from the side view. (*d*) Parameter definition of a cavitation bubble in the Venturi flow.

2. Experimental set-up

As shown in figure 1(*a*), we adopt a custom-designed Venturi tube, fabricated by thermally pulling a straight borosilicate glass tube (inner diameter: 3 mm; outer diameter: 6 mm). The throat – the narrowest section of the channel – has an inner diameter of 1.37 mm, and both upstream and downstream sections smoothly expand (upstream single-side angles of 0–3.7°, downstream of 0–3.0°) to an inner diameter of 3 mm. The total length of the tube is 214 mm, with the convergent–divergent section measuring 40.8 mm in length. The Venturi tube is integrated into a closed-loop hydraulic circuit with the flow driven by a diaphragm pump (Flojet Model D1625J7011A, 0–6.4 l min^{-1}). The pump has flow rate pulsations with a period approaching 30 ms, which is much longer than the time scale we care about in our experiments (around 1 ms), indicating the pulsations can be safely neglected. Before the experiments, an open-top acrylic reservoir is filled with approximately 2 l of deionised water. The water recirculates and does not undergo deaeration, so the concentration of air should be approaching saturated at atmospheric pressure (Tian, Li & Qian 2025). We do not vary the gas content to manipulate the naturally existing nuclei population, as its influence on nuclei properties is indirect and difficult to control in a reproducible manner. Instead, as described below, we employ a laser-based seeding approach to generate nuclei with well-defined temporal and spatial control in the flow.

A downstream absolute pressure sensor (DwyerOmega PX209-030A5V, range: 0–2 bar, accuracy: 0.25 % full scale) is installed to record the pressure used for cavitation number estimation. The cavitation number Ca is defined as $Ca = (p_d - p_v)/(0.5\,\rho\,u_{th}^2)$, where p_d is the time-averaged downstream pressure during each experimental run, $p_v = 2338.6$ Pa is the saturation vapour pressure of water at room temperature, $\rho = 998.2$ kg m^{-3} is the water density and u_{th} is the mean flow velocity at the throat section. In our experiments, the valve is always fully open, and Ca is tuned between 0.4 and 0.9 by regulating the

https://doi.org/10.1017/jfm.2026.11571 Published online by Cambridge University Press

pump power to modify u_{th}. At the location of the downstream pressure sensor, the cross-sectional area of the duct is 27.92 times larger than that at the throat, which makes the averaged velocity here very low and it varies little. Therefore, p_d varies weakly (103.9–105.9 kPa) across different operating conditions. The internal flow field is characterised by combining numerical simulation and particle tracking. Background-flow fields are obtained using steady-state simulations based on simpleFoam in OpenFOAM extended 4.0. Here, background flow refers to the pre-existing flow before the appearance of cavitation bubbles. These are experimentally validated using particle tracking results at the throat. For particle tracking, 20 μm-diameter polystyrene (PS) particles are employed as tracer particles. Further description of the methodology and results of the simulation and particle tracking is provided in Appendix A.

To realise spatio-temporally controlled cavitation nucleation, we utilise laser-induced heating of nano-sized contaminants that are inevitably present in the Venturi flow and on the wall. Some contaminants absorb laser energy and generate micro- and nanobubbles containing both non-condensable gas and vapour by localised boiling, which can act as cavitation nuclei (Rosselló & Ohl 2021; Jelenčič *et al.* 2023), see figure 1(*b*). A pulsed laser (Quantum Q2, wavelength 1064 nm, 7 ns duration) and a cylindrical convex lens (Thorlabs LJ1821L1-A, focal length 50 mm) are used to form a laser sheet with a thickness below 0.2 mm inside the Venturi tube. An upstream aperture adjusts the sheet width between 0 and 3.5 mm, with the centre positioned approximately 2.6 mm downstream of the throat. Narrower widths reduce the illuminated volume, increasing the likelihood of producing single or a few bubbles. As shown in figure 1(*c*), the laser sheet is aligned parallel to the flow direction and lies in the mid-plane of the Venturi tube. By controlling the illumination position and pulse timing, we achieve non-intrusive, high-resolution spatio-temporal control of cavitation nucleation. Nucleation within the illuminated volume, however, remains random due to the stochastic distribution of contaminants, so even under identical flow and laser conditions, different bubble types and combinations may appear.

It should be noted that not every laser shot can induce cavitation. In the illumination region, a distribution of micro- and nanobubbles with different sizes will form. In high-speed recordings, we usually cannot see them, indicating their diameters are smaller than the pixel size, which is 18.8 μm. If cavitation can nucleate from these micro- and nanobubbles, according to the classic Blake threshold (Blake 1949) for spherical bubble nuclei, the nuclei diameters should be larger than $8\sigma/[3(p_v - p)]$, where $\sigma = 0.072$ Nm^{-1} and p denote the surface tension coefficient and local pressure, respectively. For the lowest $Ca = 0.4$, the maximum diameter among the group of micro- and nanobubbles should be larger than 1.92 μm. If a laser shot does not generate micro- and nanobubbles larger than this size, then cavitation is not likely to be induced. Actually, from the perspective of a large time scale (of the order of seconds), the Venturi flow can naturally generate cavitation without the laser seeding. This is due to the pre-existing nuclei in the experimental system, possible sources could be the tracking particles in the flow (Marschall *et al.* 2003), or microbubbles (Khoo *et al.* 2020) entrapped into the system in recirculation. However, these pre-existing nuclei have little effect on our experiments. The density of the pre-existing nuclei is very low, in the time window of high-speed recording (not exceeding 1.28 ms), cavitation bubbles induced by laser-seeding and pre-existing nuclei rarely both occur.

As shown in figure 1(*c*), we use a high-speed camera (Shimadzu HPV-X2) equipped with a macro-lens (Canon MP-E 65 mm, f/2.8, 1–5×) to capture cavitation bubble motion after inception from a direction perpendicular to the flow direction. The camera operates on 200 000 or 500 000 frames per second (fps) with a diffused back illumination from a high-intensity flash lamp. The position of the nucleation plane in the Venturi tube,

https://doi.org/10.1017/jfm.2026.11571 Published online by Cambridge University Press

where the laser sheet passes, is monitored from below with a second high-speed camera (Photron AX-Mini 200, not shown here) at 40 000 fps. For better visualisation, a rectangular borosilicate glass box is placed around the Venturi tube and filled with glycerine (refractive index 1.47), which matches the refractive index of the borosilicate glass. The image distortions induced by the water–glass interface are corrected by an in-house script, which calculates the actual spatial position of each pixel based on the refractive index difference, and then reconstructs the image. Since the refractive index difference is not large, noticeable image distortion occurs only in regions close to the wall.

Figure 1(*d*) shows the parameter definition of a nearly spherical bubble with the radius R moving in the Venturi flow. The distance between the bubble centre and the throat is denoted as x. For the subsequent quantification of the effects of the flow and wall on the bubble dynamics, we denote h, R_v and h_{bl} as the distance between the bubble centre and the nearest wall, flow channel radius and boundary-layer thickness, respectively. When they refer to the moment of cavitation bubble generation, the above parameters will be denoted with 0 as the subscript. The local pressure and velocity of the background flow are denoted as p and u. Beside the cavitation number Ca, three other non-dimensional parameters are set. The non-dimensional distance from the bubble centre to the wall, $\gamma = h/R_v$, characterises the relative bubble–wall position. The non-dimensional distance from the nucleation site to the wall, i.e. $\gamma_0 = h_0/R_{v0}$, is random in every laser shot but can be measured from the high-speed images. The pressure coefficient $C_p = (p - p_d)/(0.5\,\rho\,u_{th}^2)$ represents the local pressure relative to the downstream reference pressure. The velocity coefficient $C_u = u/u_{th}$ describes the local flow velocity normalised by the averaged flow velocity at the throat. The uncertainty analysis of experiment-defined parameters is shown in Appendix B.

3. Single-bubble dynamics

We first investigate single cavitation bubble events before we address multi-bubble dynamics and their interaction. Overall, we find in experiments that a single bubble may exhibit one of three distinct fates, which are shown exemplarily in figure 2.

Figure 2(*a*) shows a bubble generated near the centreline of the flow channel ($\gamma_0 = 0.92$). Driven by the background flow and low pressure, the bubble grows while moving downstream, remaining nearly spherical due to surface tension ($t = 75\,\mu$s, $R \approx 138.3\,\mu$m). As it expands, a downstream indentation appears under the adverse pressure gradient ($t = 140\,\mu$s) and gradually deepens, flattening the bubble surface by $t = 205\,\mu$s. A re-entrant jet then develops from the downstream side, penetrates the bubble ($t = 270$–$335\,\mu$s) and forms a vapour vortex ring that eventually collapses ($t = 400\,\mu$s). Throughout the process, the bubble remains detached from the wall, representing a travelling cavitation bubble (Sato, Hachino & Saito 2003).

When the bubble is generated closer to the wall, a different fate is observed. As shown in figure 2(*b*) ($\gamma_0 = 0.36$), the bubble initially remains nearly spherical ($t = 10\,\mu$s), but by $t = 30\,\mu$s, part of its upper surface enters the boundary layer and deforms under local shear. As the bubble grows, more of its surface interacts with the boundary layer, enhancing the deformation ($t = 50\,\mu$s). Because the bubble's translational velocity exceeds that of the surrounding flow, the Kelvin–Helmholtz (K–H) instability (Podbevšek *et al.* 2021) develops along the upper interface, producing small wave-like structures (inset at $t = 50\,\mu$s). As this instability intensifies, the upper surface breaks apart, and some gas detaches from the main body and becomes entrained into the lower part of the boundary layer ($t = 70\,\mu$s) due to the lift force (Legendre & Magnaudet 1998) and bubble expansion. In this region, the entrained gases experience a weak downstream drag force due to the

https://doi.org/10.1017/jfm.2026.11571 Published online by Cambridge University Press

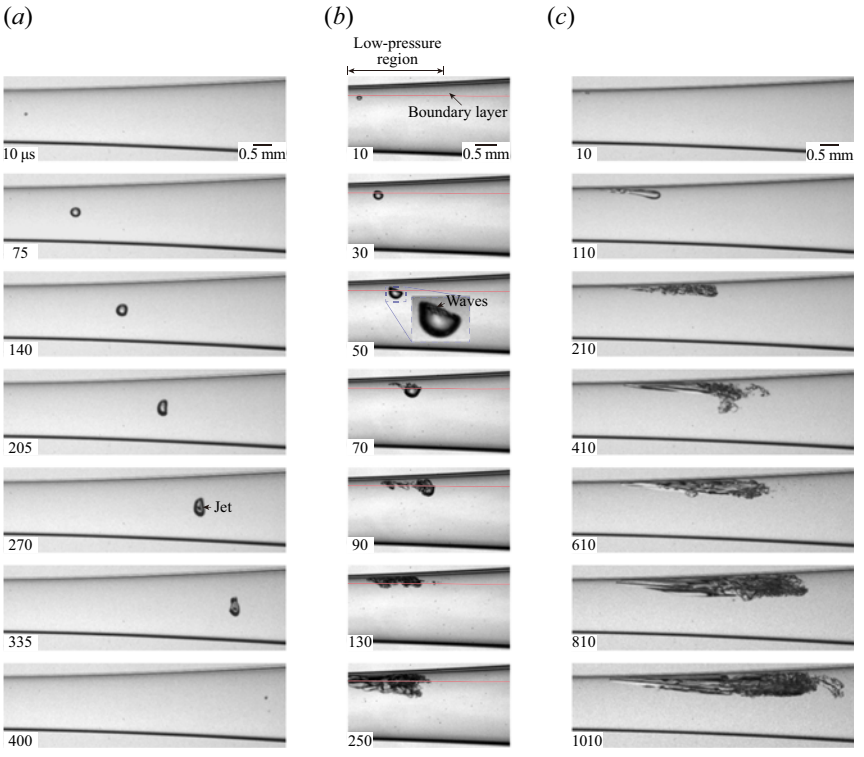


Figure 2. Fates of single bubbles. (*a*) The bubble grows, deforms and finally collapses as a travelling cavitation bubble (supplementary movie 1 are available at https://doi.org/10.1017/jfm.2026.11571). (*b*) The bubble grows and induces an attached cavity (supplementary movie 2). The red lines denote the upper flow boundary layer which is defined by 95 % mainstream velocity. The low-pressure region ($p < p_v$) is indicated by a double-headed arrow according to the simulation results of the background flow. The bubble is magnified three times in the inset for $t = 50\,\mu$s, where the alternating bright and dark contrasts on its upper surface indicate the presence of a wave structure. (*c*) The bubble occurs on the wall and directly develops into an attached cavity (supplementary movie 3).

very low flow velocity, while a strong adverse pressure gradient simultaneously exerts an upstream force. Dynamic competition between these opposing forces prevents the gases from moving downstream following the flow, but they get trapped in the low-pressure region. Since the local pressure remains below the vapour pressure, the trapped gas rapidly expands into a surface-attached cavity ($t = 90\,\mu$s), while the main bubble collapses ($t = 130\,\mu$s). Unlike travelling bubbles, this attached cavity is self-sustained ($t = 250\,\mu$s); its tail continuously sheds microbubbles, some of which are convected upstream by the adverse gradient and act as new nuclei, forming a self-sustaining cycle (Ram *et al.* 2020).

When the bubble is generated on or very close to the wall surface, it becomes fully immersed in the boundary layer. As shown in figure 2(*c*) ($\gamma_0 \approx 0$), the bubble's side facing away from the wall is exposed to shear flow and deflected downstream ($t = 10\,\mu$s), stretching into an elongated shape ($t = 110\,\mu$s). The cavity is simultaneously subjected to the downstream drag and the upstream adverse pressure gradient, and their dynamic competition keeps the cavity developing in the low-pressure region. As the interface evolves, the K–H instability develops along the shear-exposed surface, destabilising the interface ($t = 210\,\mu$s). Since the cavity stays in the low-pressure region, it keeps expanding as long as the surrounding pressure is below the vapour pressure (210–1010 µs), showing a

https://doi.org/10.1017/jfm.2026.11571 Published online by Cambridge University Press

self-sustaining nature that ultimately develops into the typical form of attached cavitation (Gawandalkar & Poelma 2024).

From the single-bubble observations, it can be concluded that a self-sustaining attached cavity forms once the bubble surface enters the boundary layer while the local pressure remains below the vapour pressure p_v. Within the low-pressure region, such cavities continue to develop and evolve into the typical attached cavitation structure. Based on the parameter definitions in figure 1(*d*), the onset condition of attached cavitation is expressed as

$$\exists\, x: \quad R(x) + h_{bl}(x) > h(x) \quad \text{and} \quad p(x) < p_v, \tag{3.1}$$

where $h_{bl}(x)$ and $p(x)$ depend on the background-flow field. In our experiments, the flow is sufficiently smooth, giving $R_v(x) - h(x) \approx R_{v0} - h_0$ during bubble growth, with R_{v0} and h_0 denoting the R_v and h values when the bubble first appears. The bubble radius $R(x)$ is predicted using the Rayleigh–Plesset (R–P) framework, which assumes a spherical bubble. In the travelling-bubble regime, the bubble remains approximately spherical throughout growth.

Due to the presence of wall constraints and background flow, correction terms are introduced to the original R–P equation, which can be written as

$$\rho\left(R\ddot{R} + \frac{3}{2}\dot{R}^2\right) - \underbrace{\rho\varphi\left(R\ddot{R} + 2\dot{R}^2\right)}_{\text{wall constraint effect}} = p_0\left(\frac{R_0}{R}\right)^{3\alpha} + p_v - p - \frac{2\sigma}{R} - \frac{4\mu\dot{R}}{R} + \underbrace{\frac{1}{4}\rho\,(u-u_b)^2}_{\text{flow effect}}, \tag{3.2}$$

where $\dot{R}$ and $\ddot{R}$ are the first and second derivatives with respect to t, p_0 is the non-condensable gas pressure inside the nucleus, R_0 is the radius of the initial nucleus, $\alpha = 1.4$ is the polytropic exponent of the gas and $\sigma = 0.072\,\mathrm{N\,m^{-1}}$ and $\mu = 0.001$ Pa s are the coefficient of surface tension and dynamic viscosity of water, respectively. Because the initial nuclei are not visible in experiments, p_0 and R_0 need to be assumed. Actually, the two parameters have little effect on bubble growth by testing, because the bubble volume will rapidly expand by several orders of magnitude larger than the initial size. The term in (3.2) for the wall constraint effect is derived from the image method in potential-flow theory, see for example Ren *et al.* (2022) and Zhang *et al.* (2023). The influence of the wall is simplified to an image bubble located on the other side of the wall. The bubble can be regarded as a point source with a potential equal to $4\pi R^2\dot{R}$, and the pressure exerted by the image bubble on the bubble is proportional to $\partial(4\pi R^2\dot{R})/\partial t = 4\pi(R\ddot{R} + 2\dot{R}^2)$, which corresponds to the form of the wall constraint effect term. For cylindrical boundaries such as the present Venturi tube, obtaining exact potential solutions is challenging. However, the wall constraint effect can still be formulated as a bubble–bubble interaction term, with an additional coefficient φ introduced and calibrated using the experimental data. Here, $\varphi = \pi CR/R_v$ following Fan, Li & Fuster (2020), and C is a constant determined by calibration. The flow effect term represents the Bernoulli pressure drop associated with the velocity difference between the bubble translational velocity u_b and the local flow velocity u (Moo *et al.* 2018), with a simplification into the average pressure on a sphere when a potential flow passes it.

Two representative cases were employed to calibrate the parameter C for the wall effect, as illustrated in figure 3. The initial conditions are set as $R|_{t=0} = R_0$ and $\dot{R}|_{t=0} = 0$. Here, R_0 is taken to be 4 μm, which is below the image resolution, but lets the nucleus be

https://doi.org/10.1017/jfm.2026.11571 Published online by Cambridge University Press

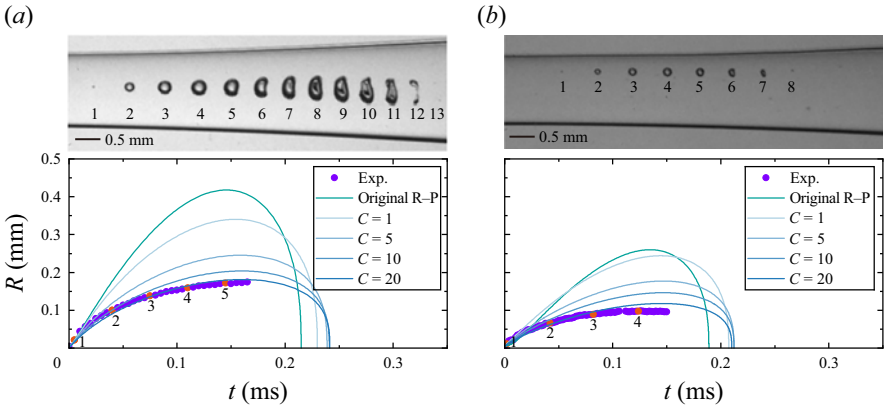


Figure 3. Prediction of bubble growth in the main flow by a R–P-type equation considering the wall confinement and flow effect. Bubble shapes at different time instants are overlaid in one composite image to show the evolution process in the Venturi flow field intuitively. The uncertainty of R, Ca and γ_0 refers to the pixel size 18.8 μm, 0.064, 0.014, respectively: (*a*) $Ca = 0.51$, $\gamma_0 = 0.92$, the time interval between different instants is 35 μs; (*b*) $Ca = 0.73$, $\gamma_0 = 0.49$, the time interval between different instants is 40 μs.

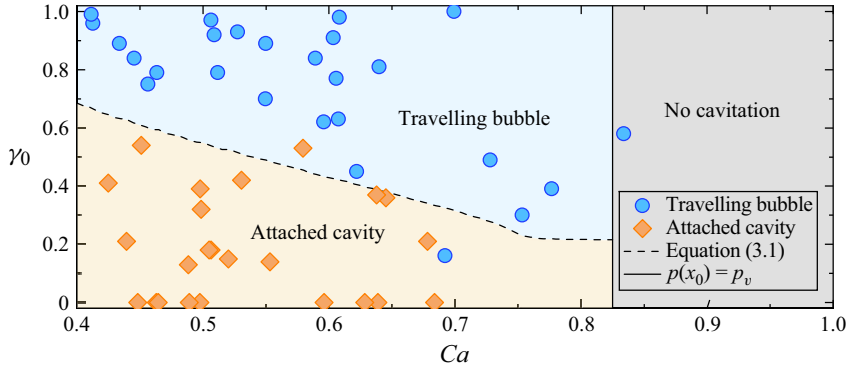


Figure 4. Experimentally derived phase diagram of cavitation regimes for single-bubble cases. Here, Ca represents the cavitation number, with the uncertainty not exceeding 0.064, and $\gamma_0 = h_0/R_{v0}$ represents the non-dimensional distance from nucleation site, with the uncertainty not exceeding 0.014.

weak enough to be activated in hydrodynamic cavitation scenarios. For p_0, we choose 10^4 Pa, which makes for good agreement between theory and experiments at the initial stage of bubble growth. It should be noted that the selected values for R_0 and p_0 affect only the early stage of bubble growth, and have little influence on the overall growth stage. The unmodified original R–P equation significantly overpredicts bubble growth. As the wall constraint effect is gradually strengthened (increasing C), the theoretical predictions approach the experimental measurements, with good agreement obtained at $C = 20$ revealing the importance of the bubble–wall interaction.

Based on (3.1) and the corresponding expressions of its variables, we obtain the phase diagram shown in figure 4. The fate of a single cavitation bubble can be expressed as a function of two basic parameters: the dimensionless initial wall distance $\gamma_0 = h_0/R_{v0}$ and the cavitation number Ca. Here, Ca characterises the susceptibility of the Venturi flow to cavitation. Lower Ca leads to larger maximum bubble sizes, thereby increasing

https://doi.org/10.1017/jfm.2026.11571 Published online by Cambridge University Press

the likelihood of penetrating into the boundary layer. The parameter γ_0, on the other hand, represents the ease with which a bubble of a given size can interact with the boundary layer; smaller γ_0 values correspond to bubbles located closer to the wall which are thus more prone to entering the boundary layer. As a result, the attached cavity regime appears in the lower-left corner of the phase diagram, corresponding to relatively small γ_0 and Ca. In contrast, the travelling-bubble regime occupies the upper-right region. To quantify this boundary, the boundary between the two regimes is evaluated at intervals of $\Delta Ca = 0.005$, and the resulting points are connected to form the theoretically predicted boundary. Specifically, the bubble radius $R(x)$ is computed using (3.2), while the boundary-layer thickness $h_{bl}(x)$ and the pressure distribution $p(x)$ are extracted from the numerical background-flow simulation. The critical value of γ_0 is then determined from the onset condition of attached cavitation given by (3.1). When Ca is large, the theoretical boundary asymptotically approaches $\gamma_0 = h_{bl}(x_0)/R_{v0}$, corresponding to bubbles generated entirely within the boundary layer. The experimental data show good agreement with the theoretically predicted regime boundary, which demonstrates the consistency and validity of the proposed model. A small number of points lie outside the nominal regime boundary, which can be attributed to finite experimental uncertainties, slight deviations from spherical bubble growth and the approximate nature of the R–P prediction. It should also be noted that a third regime, denoted as no cavitation, naturally exists. This regime is controlled solely by Ca: when Ca exceeds approximately 0.825, the local pressure at the nucleation site (2.6 mm downstream of the throat with $C_p = -0.825$) remains above p_v, thus violating the fundamental condition for hydrodynamic cavitation (Blake 1949).

4. Multiple bubbles

To move closer to typical hydrodynamic cavitation scenarios, we now consider cases involving multiple bubbles. The aim of this part is not to introduce new physical mechanisms, but to examine whether the conclusions drawn from single-bubble cases remain valid in the presence of multiple bubbles. In practice, the water used in hydraulic systems is rarely well controlled. Parameters such as gas content, including both dissolved gas, which affects gas diffusion (Arndt & Keller 1992; Li *et al.* 2023), and free gas bubbles, which directly serve as nuclei (Briançon-Marjollet *et al.* 1990; Brandner, Venning & Pearce 2022), can significantly influence the characteristics of the nuclei population. As a result, water in practical systems generally contains abundant nuclei, and the more common situation is the simultaneous inception of multiple cavitation bubbles. Here, we use the combination of nuclei seeded at different locations by laser to assemble this situation. Careful inspection of our experimental data reveals three representative cases, as shown in figure 5.

In the first case, all bubbles are travelling bubbles (figure 5*a*). In this example, three bubbles nucleate almost simultaneously and are subsequently convected downstream with the flow while growing in size. Since all bubbles remain sufficiently far from the wall, no attached cavities are formed. The evolution of these travelling bubbles is interpreted within the R–P framework. In principle, the presence of multiple bubbles introduces complex, difficult-to-quantify bubble–bubble interactions. Nevertheless, when these interactions are neglected, the R–P framework still provides a physically meaningful description of the bubble growth at a qualitative level, as demonstrated in Appendix C, where the predicted growth trends agree with the experimental observations while generally overestimating the bubble size. Within this framework, the pressure difference between the bubble interior and the surrounding liquid constitutes the dominant driving mechanism for bubble growth.

https://doi.org/10.1017/jfm.2026.11571 Published online by Cambridge University Press

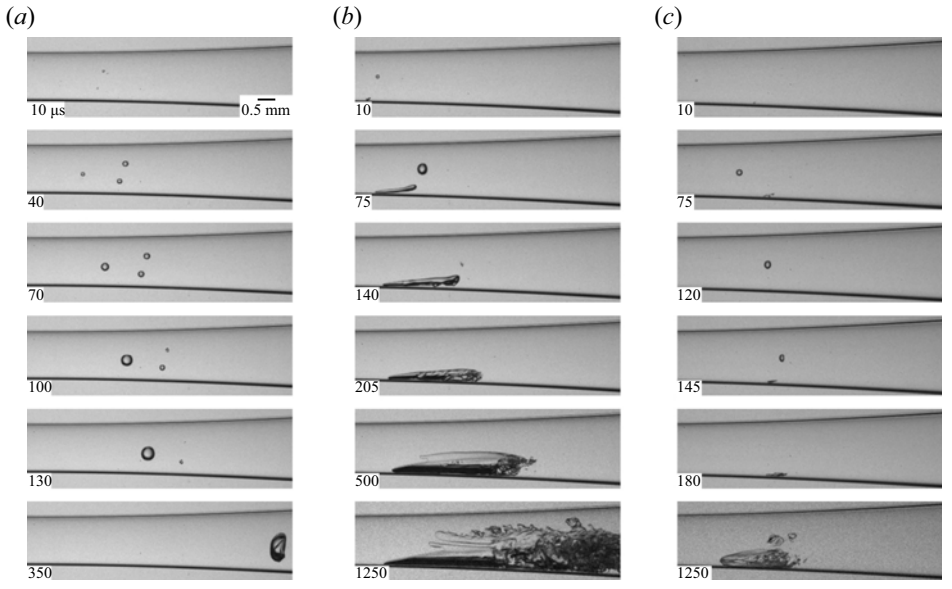


Figure 5. Fates of multiple bubbles. (*a*) Multiple travelling bubbles (supplementary movie 4). (*b*) A travelling bubble and an upstream attached cavity (supplementary movie 5). (*c*) A travelling bubble and a downstream attached cavity (supplementary movie 6). All frames share the same scale bar.

In the diffuser section of the Venturi tube, the cross-section increases gradually and, according to Bernoulli's principle, the local pressure increases downstream. As a result, bubbles initiated further downstream experience smaller pressure differentials, leading to weaker growth, smaller maximum radii and shorter lifetimes.

When attached cavities and travelling bubbles appear simultaneously, two distinct configurations are found. In the first configuration, the attached cavity is located upstream of the travelling bubble (figure 5*b*). Although the attached cavity becomes irregular in shape due to shear flow, it still follows the trend observed in figure 5(*a*): the upstream attached cavity dominates. The downstream travelling bubble collapses rapidly ($t = 140\,\mu$s), while the attached cavity remains on the wall and gradually develops into a typical attached cavitation structure ($t = 1250\,\mu$s). In this case, the attached cavity extends to the sidewall, which may be due to the small channel diameter. Here, period folds form near the cavity fore part and some of them undergo strong deformation and shedding (supplementary movie 5), which may be associated with K–H instability (Podbevšek *et al.* 2021). In the second configuration, the travelling bubble is initially located upstream of the attached cavity (figure 5*c*). Between $t = 10$ and $t = 75\,\mu$s, both the travelling bubble and the attached cavity grow, with the upstream travelling bubble attaining a larger size. Furthermore, the potential flow induced by the travelling bubble increases the pressure around the attached cavity and suppresses its growth (Ida 2009), especially when the two approach their closest separation at approximately $t = 120\,\mu$s. Nevertheless, due to the particular flow conditions within the boundary layer, the attached cavity stays put. After $t = 120\,\mu$s, the relative positions of the two structures switch, with the attached cavity now located upstream. As in the previous case (figure 5*b*), the attached cavity subsequently dominates the evolution: the travelling bubble collapses rapidly, while the attached cavity remains in the low-pressure region and develops.

The above observations show that in the competition between attached cavities and travelling bubbles, the former always finally prevail and eventually develop into attached

https://doi.org/10.1017/jfm.2026.11571 Published online by Cambridge University Press

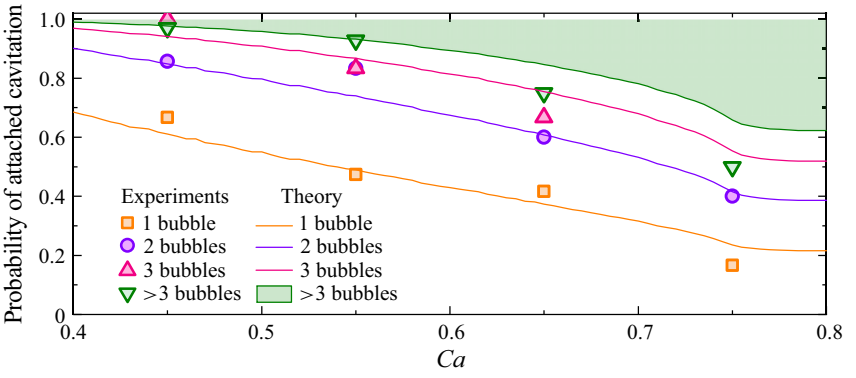


Figure 6. Probability of attached cavitation. The uncertainty of the cavitation number Ca not exceeding 0.064. The theoretical curves are based on (4.1) with different bubble numbers, i.e. n.

cavitation. Consequently, the only condition under which attached cavitation does not occur is that no attached cavity is formed at all. Assuming that nuclei are randomly distributed in the flow and, for simplicity, neglecting bubble–bubble interactions, the probability of attached cavitation can be expressed as in (4.1)

$$P_a = 1 - P_{st}^n, \tag{4.1}$$

where P_a represents the probability of attached cavitation, P_{st} represents the probability of a nucleus developing into a travelling bubble and n represents the number of bubbles in a case. For P_{st}, since the nucleation positions are assumed to be random, its value for a given Ca can be written as $P_{st} = 1 - \gamma_{0,c}$, where $\gamma_{0,c}$ refers to γ_0 lying on the boundary between two cavitation regimes in figure 4. Figure 6 shows a comparison between experimental and theoretical results. The experimental data are divided into 16 groups according to Ca (0.4–0.5, 0.5–0.6, 0.6–0.7 and 0.7–0.8) and bubble number ($n = 1$, $n = 2$, $n = 3$ and $n > 3$). Each group contains more than 10 individual cases, allowing us to statistically assess the probability of attached cavitation. The experimental results and the model overall agree well. Only for many bubbles does the model overestimate the probability of attached cavitation. This discrepancy may arise from neglecting bubble–bubble interactions, which tend to suppress each other's growth by decreasing the pressure difference between the bubble interior and the surrounding liquid (Bremond *et al.* 2006; Ida 2009). Nevertheless, the simple probabilistic model successfully captures the overall trend of the data. Importantly, the results indicate that, with only a few bubbles and at cavitation numbers commonly encountered in hydrodynamic cavitation applications, the probability of attached cavitation approaches nearly 100 %. This provides a possible explanation for why nuclei in hydrodynamic processes tend to predominantly evolve into attached cavitation.

5. Conclusions

Attached cavitation is the most common manifestation of developed hydrodynamic cavitation, yet the reason why it predominantly appears in this form was unclear. A natural way to address this question is to examine how different types of nuclei evolve under hydrodynamic cavitation conditions. However, existing experimental techniques lack the ability to precisely control cavitation nuclei in both space and time. In this work, we developed an on-demand nucleation technique for a Venturi operated below the cavitation regime. There, inevitably present micro-sized impurities in the water are rapidly heated

https://doi.org/10.1017/jfm.2026.11571 Published online by Cambridge University Press

by absorbing the energy from a pulsed laser, leading to the formation of micro- and nanobubbles. These subsequently become nuclei for hydrodynamic cavitation. Owing to the high spatio-temporal controllability of the laser, both the location and timing of nucleation events can be precisely controlled.

Using this technique, we systematically study the evolution of cavitation bubbles with various numbers, locations and cavitation numbers, Ca. We found that single bubbles can evolve into one of two regimes: travelling bubbles or attached cavities. The former originate from the direct expansion of nuclei, while the latter arise when the bubble surface enters and interacts with the boundary layer at locations where $p < p_v$. We propose a critical condition separating these two regimes and illustrate them in a phase diagram with Ca against the non-dimensional distance from nucleation site to wall, i.e. γ_0.

Extending to multiple bubbles, we find that attached cavities consistently dominate in the competition with travelling bubbles. A probabilistic model, derived from the single-bubble criterion and assuming random nucleation positions, is proposed to estimate the likelihood of attached cavitation. Despite its simplicity and the neglect of bubble–bubble interactions, the model captures the experimental trend very well. Importantly, it shows that at typical Ca, only a few bubbles are sufficient for attached cavitation to occur at nearly 100 % probability.

The present technique allows for operating Venturi flows to achieve local, on-demand hydrodynamic cavitation wherever $p < p_v$. The process may be even better controlled using suitable nanoparticles to absorb laser energy (Sharma, Ohl & Rosselló 2024), or crossed laser beams to nucleate hydrodynamic cavitation on demand three-dimensionally.

Future work can extend the present framework to account for spatially non-uniform distributions of cavitation nuclei, as commonly encountered in practical flows. For example, surface roughness and crevices on solid boundaries have long been recognised as potential sites for cavitation nuclei (Harvey *et al.* 1944; Atchley & Prosperetti 1989), and experimental studies have shown that wall-bounded nuclei can act as important sources of attached cavitation (Guennoun 2006; Groß & Pelz 2017). From the perspective of the present framework, this would lead to an increased probability of attached cavitation, which is consistent with the commonly observed prevalence of attached cavitation in hydrodynamic cavitation experiments. Such spatial inhomogeneity can be incorporated by assigning different weights to the occurrence of nuclei at different spatial locations.

Supplementary movies. Supplementary movies are available at https://doi.org/10.1017/jfm.2026.11571.

Acknowledgements. We acknowledge Professor H. Soyama for the initial version of the hydraulic system set-up.

Funding. We acknowledge financial support from DFG through the grant OH 75/12-1.

Declaration of interests. The authors report no conflict of interest.

Appendix A. Background-flow estimation

In this study, the background flow is approximated as a steady-state single-phase flow. This assumption is justified because the geometry of the Venturi flow channel varies smoothly with small single-side angles (0–3.7° and 0–3.0° for convergent and divergent parts, respectively), ensuring that the flow remains steady when cavitation is absent. Moreover, the number of bubbles generated in the present experiments is small, and their effect on the overall flow field is limited before developing into attached cavities. Therefore, the steady single-phase flow solution provides a reliable reference for estimating the background-flow field.

https://doi.org/10.1017/jfm.2026.11571 Published online by Cambridge University Press

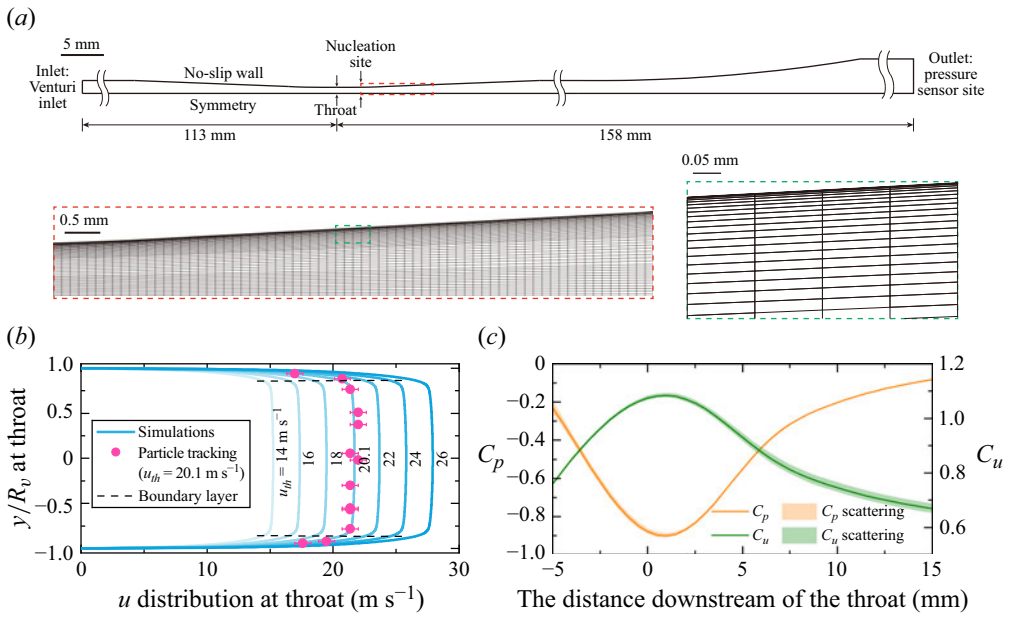


Figure 7. Background-flow estimation. (*a*) Computation domain and mesh system for numerical simulations. (*b*) Velocity profile at the throat. The particle tracking result for $u_{th} = 20.1$ ms^{-1} is used to validate the numerical velocity profiles. The thickness change of the boundary layer defined by 95 % mainstream velocity is marked by two dashed lines, which shows it slightly decreases with increasing u_{th}. (*c*) Pressure and velocity coefficient distribution in the region of interest. Here, the line and bands show the average value and data scatter of C_p or C_u for different u_{th} and across the cross-section. For C_u, only the main flow is taken into account.

The background-flow field is resolved by solving the incompressible steady-state Reynolds-averaged Navier–Stokes equations:

$$\nabla \boldsymbol{u} = 0, \tag{A1}$$

$$\nabla \cdot (\boldsymbol{u}\boldsymbol{u}) = -\nabla P + \nabla \cdot (\nu \nabla \boldsymbol{u}) + \nabla \cdot \boldsymbol{\tau}, \tag{A2}$$

where P is the pressure normalised by the water density, ν is the kinematic viscosity of water (1×10^{-6} m^{2}s^{-1}) and $\boldsymbol{\tau}$ is the Reynolds stress tensor, modelled using the k–ω shear stress transport turbulence model (Menter 1994), where k is turbulent kinetic energy and ω is specific dissipation rate. The simulation is conducted using simpleFoam in OpenFOAM extended 4.0.

The computational domain is illustrated in figure 7(*a*), covering the section from the Venturi tube inlet to the cross-section where the downstream pressure sensor is located. Owing to the geometric symmetry of the Venturi tube, only a quadrant of the circular cross-section is simulated to reduce computational cost. As the top and front views are identical, only the front view is shown here. We consider a boundary layer developed from the Venturi inlet. Thus, a uniform velocity is imposed at the inlet and a uniform pressure at the outlet. Seven steady-state cases are simulated with the throat velocity u_{th} ranging from 14 to 26 ms^{-1} in increments of approximately 2 ms^{-1}. The value of the outlet pressure can be arbitrarily selected. Since this solver only solves the relative pressure of the entire field relative to the outlet, for the convenience of calculation, we take it as 0 Pa. All solid walls are treated as no-slip boundaries, and the symmetry planes are defined as symmetry boundaries. The computational mesh contains 5422 534 cells for all cases. At

https://doi.org/10.1017/jfm.2026.11571 Published online by Cambridge University Press

the throat, one half of the diameter (0.685 mm) is resolved by 50 computational nodes, corresponding to a maximum cell size of approximately 0.022 mm in the wall-normal direction. The streamwise cell size is allowed to be larger because the Venturi tube has a much larger extent in the flow direction than in the cross-sectional direction, and the average velocity gradient along the streamwise direction is substantially weaker than it across the cross-section. Near the throat region, the cell size along the streamwise direction is below 0.1 mm. To resolve the near-wall flow accurately, the dimensionless wall distance of the first cell layer is maintained with the non-dimensional wall distance of the first mesh layer $y^+ < 1$, ensuring that the flow characteristics within the boundary layer are well captured.

Figure 7(*b*) shows the velocity distribution at the throat obtained from the numerical simulation. The flow can be divided into a mainstream region and a boundary layer, defined here by 95 % mainstream velocity. The mainstream exhibits nearly uniform velocity, while a shear flow develops within the boundary layer. For the experimental validation, PS tracer particles with a diameter d_p of approximately 20 µm and a density ρ_p of 1.05 g cm^{-3} are seeded into the flow at the operating condition corresponding to $u_{th} = 20.1$ ms^{-1}. The associated Stokes number is defined as $St = \tau_p/\tau_f$, where $\tau_p = \rho_p d_p^2/(18\mu)$ is the particle relaxation time and $\tau_f = l_{con}/u_{th}$ is the characteristic flow time scale, where $l_{con} = 19.8$ mm is the length of the convergent part. Then it yields $St = 0.024$. This form of St reflects the ability of particles to follow the acceleration of Venturi flow through the convergent part. Although St is not small enough to reach the ideal range of $<10^{-3}$ (Adrian & Westerweel 2011), it is still applicable enough to capture such smooth and nearly steady flow (Gebensleben, Reuter & Ohl 2025), without concern for the detailed turbulent structure. Near the throat, the tracer particles move essentially in a one-dimensional manner. The particle velocities are obtained by manually tracking multiple particles at different wall-normal positions in the high-speed images. Their displacement over a given number of frames is measured, and the corresponding velocities are computed, with the uncertainty arising from the pixel size; the uncertainty analysis can be found in Appendix B. As shown in figure 7(*b*), the velocity measurements by particle tracking agree very well with the numerical simulation in the Reynolds-averaged sense, demonstrating the high reliability of the simulated background flow. Moreover, the boundary-layer thickness at the throat shows little variation among different velocity cases, with a single-side thickness decreasing from 0.142 to 0.134 R_v with u_{th} from 14 to 26 ms^{-1}. This small decrease is supported by an empirical scaling law, which indicates that the turbulent boundary-layer thickness scales approximately with the Reynolds number to the power of -1/5 (White & Majdalani 2006; Schlichting & Gersten 2016).

Numerically derived distributions of the velocity coefficient C_u in the main flow and the pressure coefficient C_p are presented in figure 7(*c*). Both C_p and C_u show very small variations across the cross-section and different u_{th}, indicating that they can be represented by a single value at each streamwise position. The narrow shaded bands in figure 7(*c*) illustrate these small differences across different positions and flow conditions. Therefore, C_p and C_u can be reasonably expressed as functions of the streamwise coordinate x alone.

Appendix B. Uncertainty analysis

The uncertainties of the measured quantities are estimated by considering both instrumental and statistical contributions. For convenience, relative uncertainties are first derived for propagation, while the final uncertainties are reported in absolute form.

https://doi.org/10.1017/jfm.2026.11571 Published online by Cambridge University Press

B.1. *Flow velocity u*

The flow velocity is obtained from particle tracking as $u = (x_i - x_{i-1})/\Delta t$, where x_i and x_{i-1} denote two consecutive particle positions and Δt is the corresponding time interval. The spatial resolution is $\Delta x = 0.5$ pixel, corresponding to 9.4 μm. The velocity is evaluated over a time interval of $t = 40$ μs, and the temporal resolution error is negligible. The instrumental uncertainty of the velocity is therefore estimated as $\Delta u_{ins} = 2\Delta x/t \approx 0.47\ \mathrm{ms}^{-1}$.

Typically, the velocity is evaluated from 5 tracked particles. The statistical uncertainty of the mean velocity is estimated using the Student's t distribution at a 95 % confidence level, yielding $\Delta u_{st} \approx 1.24\, s_u$, where s_u is the sample standard deviation. In the present measurements, s_u does not exceed $0.3\ \mathrm{ms}^{-1}$, giving $\Delta u_{st} \leqslant 0.37\ \mathrm{ms}^{-1}$. The total uncertainty of the velocity is obtained as $\Delta u_{tot} = \sqrt{(2/3\Delta u_{ins})^2 + (\Delta u_{st})^2} \leqslant 0.49\ \mathrm{ms}^{-1}$.

B.2. *Cavitation number Ca*

The cavitation number is defined as $Ca = (p_d - p_v)/(0.5\rho u_{th}^2)$. The pressure is measured using a pressure transducer with an uncertainty of $\Delta p = \pm 500$ Pa. Since p_d is defined as the time-averaged value within a single experimental run, only the instrumental uncertainty of the pressure is considered.

The instrumental uncertainty of the cavitation number is estimated as $\Delta Ca_{ins} = Ca((\Delta p/p_d - p_v) + 2(\Delta u_{ins}/u_{th}))$. Using conservative bounds of the experimental conditions, the instrumental contribution to the total uncertainty is estimated as $(2/3)\Delta Ca_{ins} \leqslant 0.043$. The statistical uncertainty of the cavitation number arises from the statistical uncertainty of the velocity, given by $\Delta Ca_{st} = Ca(2(\Delta u_{st}/u_{th})) \leqslant 0.048$. The total uncertainty of the cavitation number is therefore $\Delta Ca_{tot} = \sqrt{(2/3\Delta Ca_{ins})^2 + (\Delta Ca_{st})^2} \leqslant 0.064$.

B.3. *Non-dimensional distance from nucleation site to wall γ_0*

The non-dimensional distance is defined as $\gamma_0 = h_0/R_{v0}$, where h is the distance between the nucleation site and the wall, and R_{v0} is the throat radius. The uncertainty in h_0 is determined by the spatial resolution, taken as half a pixel (9.4 μm). The corresponding uncertainty in γ_0 is $\Delta\gamma_0 = \Delta h_0/R_{v0} \approx 0.014$. Since γ_0 corresponds to a single geometrical measurement for each event, only instrumental uncertainty is considered.

Appendix C. Bubble growth prediction for example case of multiple bubbles without considering bubble–bubble interaction

To assess, in a simplified manner, the influence of bubble–bubble interactions on the applicability of the R–P framework, we consider the representative multiple travelling-bubble case shown in figure 5(*a*).

In principle, each cavitation bubble induces an additional pressure field that affects the dynamics of neighbouring bubbles, which can be incorporated into the R–P equation through a bubble–bubble interaction term derived from potential-flow theory by modelling each bubble as a point source (Moo et al. 2018). However, in the present problem, multiple bubbles evolve simultaneously in close proximity to complex solid boundaries, giving rise to a highly intricate system of image bubbles. Under such conditions, obtaining a closed-form expression for the bubble–bubble interaction terms becomes impractical. We therefore neglect bubble–bubble interactions and predict the growth of the three bubbles using (3.2).

https://doi.org/10.1017/jfm.2026.11571 Published online by Cambridge University Press

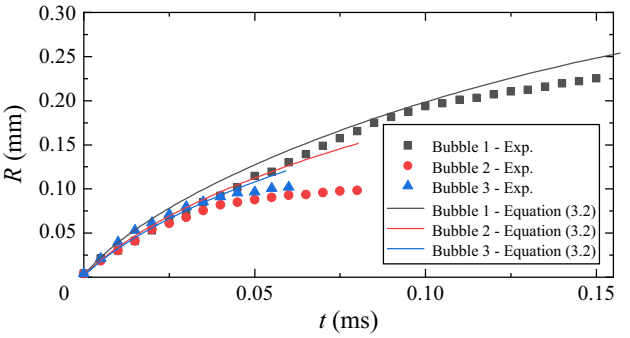


Figure 8. Prediction of bubble growth for the case of figure 5(*a*) using (3.2). A larger bubble number means the location of generation is further downstream. Initial condition: $R\,|_{t=0}= 0.004$ mm, $\mathrm{d}R/\mathrm{d}t\,|_{t=0}= 0$, $p_0 = 10\,000$ Pa. The experimental uncertainty of R refers to the pixel size 18.8 μm.

The initial conditions are set as $R\,|_{t=0}= 0.004$ mm and $\mathrm{d}R/\mathrm{d}t\,|_{t=0}= 0$, with $p_0 = 10\,000$ Pa. The background pressure distribution used in the calculation corresponds to the same experimental case shown in figure 5(*a*). The resulting comparison between the predicted and experimentally measured bubble radii is shown in figure 8.

The results indicate that, for this relatively sparse multiple-bubble configuration, the R–P framework without bubble–bubble interactions remains qualitatively valid and captures the overall growth trends of the bubbles. However, the predicted radii are systematically overestimated. This discrepancy becomes more pronounced for bubbles 2 and 3 as bubble 1 grows, highlighting the increasing influence of bubble–bubble interactions. Here, a larger bubble number means the location of generation is further downstream. These observations suggest that, at a qualitative level, bubble growth in multiple-bubble hydrodynamic cavitation can still be interpreted within the R–P framework by recognising the pressure difference between the bubble interior and the background flow as the dominant driving mechanism, while bubble–bubble interactions act to reduce the effective growth rate.

At a quantitative level, an accurate description of multiple-bubble hydrodynamic cavitation requires resolving complex interactions between bubbles and solid boundaries. The most promising route towards such a description is advanced numerical simulation. To the best of our knowledge, fully resolved simulations of even a single hydrodynamic cavitation bubble barely exist. We are currently developing, together with collaborators, numerical models aimed at resolving the dynamics of a single and a small number of hydrodynamic cavitation bubbles. A quantitative treatment of multiple-bubble interactions is therefore left for future work.

References

Adrian, R.J. & Westerweel, J. 2011 *Particle Image Velocimetry*. Cambridge University Press.

Agarwal, K., Ram, O., Lu, Y. & Katz, J. 2023 On the pressure field, nuclei dynamics and their relation to cavitation inception in a turbulent shear layer. *J. Fluid Mech.* **966**, A31.

Allan, E.S.C., Barbaca, L., Russell, P.S., Venning, J.A., Pearce, B.W. & Brandner, P.A. 2025 Cavitation nucleation dynamics in structured turbulence. *J. Fluid Mech.* **1011**, R4.

Arndt, R.E.A. 1981 Cavitation in fluid machinery and hydraulic structures. *Annu. Rev. Fluid Mech.* **13** (1), 273–326.

Arndt, R.E.A. & Keller, A.P. 1992 Water quality effects on cavitation inception in a trailing vortex. *J. Fluids Engng* **114** (3), 430–438.

Atchley, A.A. & Prosperetti, A. 1989 The crevice model of bubble nucleation. *J. Acoust. Soc. Am.* **86** (3), 1065–1084.

https://doi.org/10.1017/jfm.2026.11571 Published online by Cambridge University Press

BLAKE, F.G., Jr. 1949 The onset of cavitation in liquids: I. *Tech. Rep. 12*. Acoustics Research Laboratory, Harvard University.
BRANDNER, P.A., VENNING, J.A. & PEARCE, B.W. 2022 Nucleation effects on cavitation about a sphere. *J. Fluid Mech.* **946**, A1.
BREMOND, N., ARORA, M., OHL, C.-D. & LOHSE, D. 2006 Controlled multibubble surface cavitation. *Phys. Rev. Lett.* **96** (22), 224501.
BRIANÇON-MARJOLLET, L., FRANC, J.-P. & MICHEL, J.-M. 1990 Transient bubbles interacting with an attached cavity and the boundary layer. *J. Fluid Mech.* **218**, 355–376.
CHATTERJEE, D. & ARAKERI, V.H. 2004 Some investigations on the use of ultrasonics in travelling bubble cavitation control. *J. Fluid Mech.* **504**, 365–389.
DULAR, M. & PETKOVŠEK, M. 2015 On the mechanisms of cavitation erosion–coupling high speed videos to damage patterns. *Exp. Therm. Fluid Sci.* **68**, 359–370.
FAN, Y., LI, H. & FUSTER, D. 2020 Optimal subharmonic emission of stable bubble oscillations in a tube. *Phys. Rev. E* **102** (1), 013105.
FRANC, J.P. & MICHEL, J.M. 1985 Attached cavitation and the boundary layer: experimental investigation and numerical treatment. *J. Fluid Mech.* **154**, 63–90.
GAWANDALKAR, U.U. & POELMA, C. 2024 The characteristics of bubbly shock waves in a cavitating axisymmetric venturi via time-resolved X-ray densitometry. *J. Fluid Mech.* **988**, A34.
GEBENSLEBEN, D., REUTER, F. & OHL, C.D. 2025 Single cavitation bubble dynamics in a confined planar flow. *Intl J. Multiphase Flow* **188**, 105224.
GROSS, T.F. & PELZ, P.F. 2017 Diffusion-driven nucleation from surface nuclei in hydrodynamic cavitation. *J. Fluid Mech.* **830**, 138–164.
GUENNOUN, M.F. 2006 Étude physique de l'apparition et du développement de la cavitation sur une aube isolée. *PhD thesis*, EPFL.
HARVEY, E.N., BARNES, D.K., MCELROY, W.D., WHITELEY, A.H., PEASE, D.C. & COOPER, K.W. 1944 Bubble formation in animals. I. Physical factors. *J. Cell. Compar. Physl.* **24** (1), 1–22.
IDA, M. 2009 Multibubble cavitation inception. *Phys. Fluids* **21** (11), 113302.
JELENČIČ, M., ORTHABER, U., MUR, J., PETELIN, J. & PETKOVŠEK, R. 2023 Evidence of laser-induced nanobubble formation mechanism in water. *Ultrason. Sonochem.* **99**, 106537.
KHOO, M.T., VENNING, J.A., PEARCE, B.W., TAKAHASHI, K., MORI, T. & BRANDNER, P.A. 2020 Natural nuclei population dynamics in cavitation tunnels. *Exp. Fluids* **61** (2), 34.
LEGENDRE, D. & MAGNAUDET, J. 1998 The lift force on a spherical bubble in a viscous linear shear flow. *J. Fluid Mech.* **368**, 81–126.
LEIGHTON, T.G., FARHAT, M., FIELD, J.E. & AVELLAN, F. 2003 Cavitation luminescence from flow over a hydrofoil in a cavitation tunnel. *J. Fluid Mech.* **480**, 43–60.
LI, C.Y. & CECCIO, S.L. 1996 Interaction of single travelling bubbles with the boundary layer and attached cavitation. *J. Fluid Mech.* **322**, 329–353.
LI, M., LIU, J., LI, J., XIANG, B., MANICA, R. & LIU, Q. 2022 Enhancement of selective fine particle flotation by microbubbles generated through hydrodynamic cavitation. *Powder Technol.* **405**, 117502.
LI, Z., ZUO, Z. & QIAN, Z. 2023 Diffusion-driven periodic cavitation bubbling from a harvey-type crevice in shear flows. *Phys. Fluids* **35** (10), 102112.
MARSCHALL, H.B., MØRCH, K.A., KELLER, A.P. & KJELDSEN, M. 2003 Cavitation inception by almost spherical solid particles in water. *Phys. Fluids* **15** (2), 545–553.
MENTER, F.R. 1994 Two-equation eddy-viscosity turbulence models for engineering applications. *AIAA J.* **32** (8), 1598–1605.
MOO, J.S., MAYORGA-MARTINEZ, C.C., WANG, H., TEO, W.Z., TAN, B.H., LUONG, T.D., GONZALEZ-AVILA, S.R., OHL, C.D. & PUMERA, M. 2018 Bjerknes forces in motion: long-range translational motion and chiral directionality switching in bubble-propelled micromotors via an ultrasonic pathway. *Adv. Funct. Mater.* **28** (25), 1702618.
NÖPEL, J.A. & AYELA, F. 2023 Experimental evidences of radicals production by hydrodynamic cavitation: a short review. *C. R. Chim.* **26** (G2), 157–166.
PENNINGS, P.C., BOSSCHERS, J., WESTERWEEL, J. & VAN TERWISGA, T.J.C. 2015 Dynamics of isolated vortex cavitation. *J. Fluid Mech.* **778**, 288–313.
PODBEVŠEK, D., PETKOVŠEK, M., OHL, C.D. & DULAR, M. 2021 Kelvin–Helmholtz instability governs the cavitation cloud shedding in venturi microchannel. *Intl J. Multiphase Flow* **142**, 103700.
RAM, O., AGARWAL, K. & KATZ, J. 2020 On the mechanisms that sustain the inception of attached cavitation. *J. Fluid Mech.* **901**, R4.
REN, Z., ZUO, Z., WU, S. & LIU, S. 2022 Particulate projectiles driven by cavitation bubbles. *Phy. Rev. Lett.* **128** (4), 044501.

https://doi.org/10.1017/jfm.2026.11571 Published online by Cambridge University Press

ROSSELLÓ, J.M. & OHL, C.D. 2021 On-demand bulk nanobubble generation through pulsed laser illumination. *Phys. Rev. Lett.* **127** (4), 044502.

ROSSELLÓ, J.M. & OHL, C.D. 2023 Clean production and characterization of nanobubbles using laser energy deposition. *Ultrason. Sonochem.* **94**, 106321.

SATO, K., HACHINO, K. & SAITO, Y. 2003 Inception and dynamics of traveling-bubble-type cavitation in a venturi. In *Fluids Engineering Division Summer Meeting*, vol. 36967, pp. 279–285. ASME.

SCHLICHTING, H. & GERSTEN, K. 2016 *Boundary-Layer Theory*. Springer.

SHARMA, Y., OHL, C.D. & ROSSELLÓ, J.M. 2024 Nanobubble nucleation by pulsed laser illumination of colloidal gold nanoparticles. *Sci. Rep.* **14** (1), 1–12.

TIAN, X., LI, Z. & QIAN, Z. 2025 Effect of dissolved air content on attached cavitation in a venturi section. *Phys. Fluids* **37** (1), 013355.

VENNING, J.A., PEARCE, B.W. & BRANDNER, P.A. 2022 Nucleation effects on cloud cavitation about a hydrofoil. *J. Fluid Mech.* **947**, A1.

WHITE, F.M. & MAJDALANI, J. 2006 *Viscous Fluid Flow*, vol. 3. McGraw-Hill.

ZHANG, A., LI, S., CUI, P., LI, S. & LIU, Y. 2023 A unified theory for bubble dynamics. *Phys. Fluids* **35** (3), 033323.

ŠARC, A., STEPIŠNIK-PERDIH, T., PETKOVŠEK, M. & DULAR, M. 2017 The issue of cavitation number value in studies of water treatment by hydrodynamic cavitation. *Ultrason. Sonochem.* **34**, 51–59.

https://doi.org/10.1017/jfm.2026.11571 Published online by Cambridge University Press